

# Noema: Hardware-Efficient Template Matching for Neural Population Pattern Detection

Ameer M. S. Abdelhadi  
University of Toronto  
ameer.abdelhadi@utoronto.ca

Eugene Sha  
University of Toronto  
eugene.sha@mail.utoronto.ca

Ciaran Bannon  
University of Toronto  
ciaran.bannon@utoronto.ca

Hendrik Steenland  
NeuroTek Innovative Technology Inc.  
wsneurotek@gmail.com

Andreas Moshovos  
University of Toronto  
moshovos@ece.utoronto.ca

## ABSTRACT

Repeating patterns of activity across neurons is thought to be key to understanding how the brain represents, reacts, and learns. Advances in imaging and electrophysiology allow us to observe activities of groups of neurons in real-time, with ever increasing detail. Detecting patterns over these activity streams is an effective means to explore the brain, and to detect memories, decisions, and perceptions in real-time while driving effectors such as robotic arms, or augmenting and repairing brain function. *Template matching* is a popular algorithm for detecting recurring patterns in neural populations and has primarily been implemented on commodity systems. Unfortunately, template matching is memory intensive and computationally expensive. This has prevented its use in portable applications, such as neuroprosthetics, which are constrained by latency, form-factor, and energy. We present *Noema* a dedicated template matching hardware accelerator that overcomes these limitations. *Noema* is designed to overcome the key bottlenecks of existing implementations: *binning* that converts the incoming bit-serial neuron activity streams into a stream of aggregate counts, *memory storage* and *traffic* for the templates and the binned stream, and the extensive use of floating-point arithmetic. The key innovation in *Noema* is a reformulation of template matching that enables computations to proceed progressively as data is received without binning while generating numerically identical results. This drastically reduces latency when most computations can now use simple, area- and energy efficient bit- and integer-arithmetic units. Furthermore, *Noema* implements template encoding to greatly reduce template memory storage and traffic. *Noema* is a hierarchical and scalable design where the bulk of its units are low-cost and can be readily replicated and their frequency can be adjusted to meet a variety of energy, area, and computation constraints.

## ACM Reference Format:

Ameer M. S. Abdelhadi, Eugene Sha, Ciaran Bannon, Hendrik Steenland, and Andreas Moshovos. 2021. Noema: Hardware-Efficient Template Matching for Neural Population Pattern Detection. In *MICRO'21: 54th Annual*

Permission to make digital or hard copies of all or part of this work for personal or classroom use is granted without fee provided that copies are not made or distributed for profit or commercial advantage and that copies bear this notice and the full citation on the first page. Copyrights for components of this work owned by others than ACM must be honored. Abstracting with credit is permitted. To copy otherwise, or republish, to post on servers or to redistribute to lists, requires prior specific permission and/or a fee. Request permissions from [permissions@acm.org](mailto:permissions@acm.org).

*MICRO '21, October 18–22, 2021, Virtual Event, Greece*

© 2021 Association for Computing Machinery.

ACM ISBN 978-1-4503-8557-2/21/10...\$15.00

<https://doi.org/10.1145/3466752.3480121>

*IEEE/ACM International Symposium on Microarchitecture (MICRO '21), October 18–22, 2021, Virtual Event, Greece. ACM, New York, NY, USA, 13 pages.*  
<https://doi.org/10.1145/3466752.3480121>

## 1 INTRODUCTION

There are approximately 86 billion neurons in the human brain with trillions of connections. These neurons generate and transmit electrophysiological signals to communicate within and between brain regions. More than two centuries ago Galvani pioneered the study of bioelectricity using simple electrode technologies applied to the frog nerve and muscle [25]. Our understanding of the electrical currents of nerves has since greatly expanded using increasingly refined techniques [32, 34] resulting in modern neuroprobe technologies including the tetrode, Michigan silicon probes, Utah microelectrode arrays, Thomas electrodes, electrode drive mechanisms [70], and neuropixel probes [36]. More recently, genetic techniques manipulate neurons to express calcium indicators so neuron bioelectricity could be imaged [80]. Collectively, these new technologies enable us to capture the activity of ever increasing populations of neurons. Ultimately, the signals these probes capture, are digitized and processed in the digital domain.

Several challenges remain for the development of a widely accepted neuron-based brain machine interface, including electrode bio-compatibility, large-scale sampling of neuronal data, real-time pre-processing and storage of the data, “sorting” neural spike activity, detecting neural patterns, and selecting the relevant patterns [57, 69, 77]. These challenges require innovation in several disciplines. Undergoing efforts in electrode bio-compatibility include coatings [69, 76, 78], avoiding the destruction of vasculature [53], and the development of electrodes made from neural tissue itself [9]. Attempts have been made in the calcium imaging domain via some level of genetic manipulation [19]. However, invasive imaging methods tend to have better long term signal stability [10, 83], as demonstrated in animal models, and represent a real future potential for neuron detection.

As advancements in sensing technologies accelerate, the downstream digital processing stack must also grow for the overall system to keep pace. The success of such systems hinges upon meeting latency, throughput, energy, and form-factor constraints when processing the raw neural data stream. While innovations are still to occur, the algorithms employed for processing have become widely adopted and are sufficiently stable for a variety of applications. Existing implementations are predominantly in-house, most of which

are only appropriate for off-line analysis on a limited number of neurons. Such implementations often fail to meet the aforementioned constraints for portable applications such as neuroprosthetics. Developing computing systems to meet the needs of current and future neuron-based brain machine interfaces can be highly inaccessible due to the need for multidisciplinary collaboration. The time and effort required to learn to “speak” the language of other fields and to hone in on the most relevant features are major up-front costs necessitating strong commitments and incentives from all parties involved. This is even more challenging when coupled with the prototype development costs of custom hardware, and its eventual deployment to scale.

As a result of such a collaborative effort, we report our experience in analyzing and developing a custom hardware platform to meet the requirements of a major component of such systems: *pattern matching*. The goal of pattern matching is to detect if a certain pattern of neuron activity occurs over some short period of time. This processing is purely in the digital domain, and its input are bit streams each representing the activity in time of one or more neurons. Such patterns of neuron activity are thought to be key to understanding how the brain represents, reacts, and learns from the external environment [59, 60]: Neuronal populations have been found to have reliable motor activation, replay patterns of activity in association with previous experiences during wakefulness [16, 37], sleep [20, 23, 37, 43, 46, 62, 74] and intrinsically [13, 48, 49] during field oscillation. During sleep, these patterns can recur at accelerated rates [23, 43, 46, 54], and even in reverse order [24]. The “memory” replay of these patterns can occur across various brain regions and in coordination [35, 58]. Analytic output from populations of neurons can effectively drive robotic limbs [15, 42, 50]. Taken together, detecting patterns of neuronal populations is an effective means to explore and predict the brain. Pattern matching algorithms could detect memories, decisions, emotions, perceptions in real-time while driving effectors such as robotic arms, memory retrieval or even augment brain function. As most of these applications need to be *untethered*, where the device can be carried by the subject with a portable power source, a small form factor and low power consumption (less than 2W [53, 66]) are highly desirable.

As we will later expand upon, the current computational and memory demands of pattern matching only worsen with the rapid increase in the number of neurons simultaneously recorded. Recent estimates range from 3,000 neurons [72] when recording with electrophysiological signals [36] to upwards of a million when recording from optical signals [39]. Accordingly, there is a growing need for accelerating algorithms and dedicated devices to process patterns of neural data fast enough for real-time applications. Pattern matching is challenging since a pattern is *not* an exact sequence of neuronal activity that repeats perfectly every time. Instead, pattern detection has to cope with inherently “noisy” neuron activity signals to assess patterns with some level of certainty. A range of algorithms have been used to assess patterns of activity in populations of neurons and include; Bayesian decoding [17, 29], recurrent artificial neural networks [15], explained variance [41, 74], correlations of cell pairs [16, 37] and template matching with the Pearson’s Correlation Coefficient, or *Template Matching* for short [21, 23, 46, 51, 62, 74, 75, 79, 81]. The feasibility of a real-time pattern detection system has been demonstrated with

a Bayesian decoding scheme with 128 electrodes [17, 29] while studies involving recurrent artificial neural networks relied upon 32 neuron recordings [15]. A desktop-class GPU could process 2000 channels of data input in less than 250msec [33]. Unfortunately, in real-time applications a 50msec response is highly desirable [18].

The memory and computation needs of Template Matching vary depending on the number of sampled neurons, and the number and size of the pre-recorded templates. We study representative configurations for a broad spectrum of applications (Table 1). At the lower-end are applications possible with existing commodity hardware (albeit still not portable), whereas at the high-end are applications that are not practical today but for which the neuroprobe technology is within reach. Inspired by previous work in template matching [23, 46, 62, 74] Section 5 presents  $PCC_{BASE}$ , a highly optimized vector-unit-based implementation of template matching.  $PCC_{BASE}$  is representative of current implementations. However, our implementation optimizes memory and compute organization to best match the needs of each configuration studied, some of which far exceed previously published studies. For the configurations studied, the computation requirements vary from 600MOPS (operations, defined as an arithmetic operation) to 1.7GOPS *per template*. The on-chip storage of  $PCC_{BASE}$  ranges from 40KB for our lowest-end configuration to 160MB for the most demanding one. We highlight the following observations about past implementations of template matching as motivation for our optimized design. Existing implementations of template matching implement Pearson’s Correlation as originally proposed. To do so they first bin the input bit-streams of activity, into streams of aggregate integer counts. The core computation initiates only *after* a full time window of relevant samples (equal to the template’s time dimension) has been received, impacting memory storage needs and traffic and worse response times. Many of these are floating-point computations. As Subsection 5.4 corroborates, even desktop-class GPUs fail to meet real-time latency for more demanding applications.

As **our main contribution**, Section 3 presents *Noema*, a hardware accelerator that greatly reduces area and energy costs compared to  $PCC_{BASE}$  while maintaining real-time performance. *Noema* reduces costs and up-time for the configurations that are practical with  $PCC_{BASE}$ , and supports even more demanding configurations and thus can enable further advances in neuroscience. At the core of *Noema* is a decomposition of the template matching algorithm where the bulk of the computations are performed using simple, low-cost, specialized *bit-level* operations. More importantly, in stark contrast with existing implementations, *Noema* performs its bulk of the computations as it receives samples bit-by-bit, producing the final output only a few cycles after the last bit in the relevant window is seen. Besides reducing latency, *Noema*’s approach avoids having to temporarily store the incoming stream, saving memory storage and traffic. To further reduce memory storage and traffic, we observe that templates naturally exhibit a geometric-like distribution in their value content which is heavily biased towards very low magnitude values. We equip *Noema* with a hardware-efficient decoder to greatly reduce template storage and traffic with little energy and area cost. For the most demanding configuration, *Noema* needs 34MB of on-chip storage. The simplicity and tiny area cost of the processing units of *Noema* enables tuning the operating frequency to improve power efficiency via partitioning and replication

at a minimal area overhead (see Subsection 3.6). We study *Noema* and  $PCC_{BASE}$  as custom hardware implementations performing synthesis and layout and also summarize the characteristics of an FPGA implementation of *Noema*. We use our template compression for all designs. We also study the performance of our decomposed template matching implementation over commodity hardware: an embedded class general purpose processor (CPU), and a desktop class graphics processor (GPU).

This work contributes a computer-architect-targeted introduction to a typical neuroprobe processing pipeline with the emphasis being on a critical component, pattern matching, along with use cases representative of a range of applications. This introduction includes a detailed description of a popular template matching implementation and a discussion of the challenges faced by implementations over a variety of commodity platforms. These summaries motivate *Noema* a hardware-friendly reformulation of template matching.

We highlight the following takeaways and innovations:

- As presented and currently implemented, Pearson’s Correlation requires storing the templates and a correspondingly large window of the input incoming stream in binned form. These matrices are costly, e.g., 1.24Gb each.
- The computation needs also grow and reach 1.6TOPs (mostly floating-point) for the largest configuration studied.
- Computation latency and throughput are the primary challenges as the computation has to finish within strict constraints (5 msec per window).
- *Noema* reformulates the computation so that the input streams are consumed as they are received bit-by-bit, obviating the need for buffering the input. This: 1) greatly reduces memory needs, and 2) allows *Noema* to meet real-time response times as it leaves very little computation to be done *after* a window’s worth of input is received (throughput is now the key constraint).
- *Noema*’s formulation enables the use of tiny bit-serial units for the bulk of the computation. *Noema* replicates and places these units near the template memory banks (near memory compute). This enables high data parallel processing and scaling at low cost.
- *Noema* uses a hierarchical, tree-like arrangement of the compute units where floating point and expensive operations are needed sparingly.
- *Noema* exploits the sparsity of the template content via per bank, light-weight, hardware friendly decompression units. Templates are compressed in advance in software.
- *Noema* can greatly reduce power by gating accesses to the template memory, as the input bit stream is sparse and the inputs are processed a single bit at a time.

We highlight the following experimental findings:

- (1) *Noema* can meet the real-time requirements: Depending on the configuration it requires 683mw to 1.2W and occupies respectively  $0.11mm^2$  to  $205mm^2$  in a 65nm process node.
- (2) *Noema*’s template compression reduces template memory size by at least  $2.79\times$  (most demanding conf.).
- (3) An FPGA implementation meets real time requirement only for some of the configurations studied.
- (4) An embedded class CPU fails real-time constraints for all configurations while a desktop class GPU fails for the most demanding ones.

## 2 BACKGROUND AND PRELIMINARIES

Fig. 1 shows a high-level neural processing system for pattern detection. Using neuroprobes, electrophysiological spikes of a living brain tissue are continuously sampled and processed initially as *analog* signals. This *spike detection and sorting* stage produces a time-ordered digital stream of *binary indicators* (0 or 1). There is one indicator  $q_n[t]$  per neuron  $n$  and per time step  $t$ . The typical sampling rate of neural spikes is 30KHz [26, 30, 56] resulting in a 30,000 *bits/sec* stream per neuron. Today, applications use neuroprobes capable of capturing the activity of several hundreds of neurons [36, 72]. However, the technology is rapidly evolving and neuroprobes capturing thousands and eventually millions of neuron are within sight [40, 52].

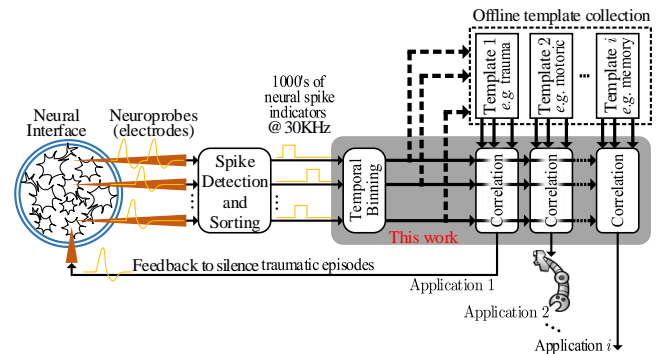


Figure 1: Abstraction of template matching applications.

Pattern detection relies on the observation that certain events of interest such as memories, decisions, or perceptions, manifest as *patterns* in the neuron stream [35, 58]. Informally, as Fig. 1 depicts, in these applications, patterns of interest have been pre-recorded and are continuously compared against the incoming indicator stream. Naturally, this pattern matching process is not precise and has to rely on some *stochastic* proximity metric. This work targets applications where pattern matching occurs in real time. Relevant applications include memory detection in real time for prosthetic control. a *pattern detection latency* of 50ms is desirable [18]. This is defined as the time needed to detect the pattern once receiving the very last indicator. We will use the term *latency* to refer to the pattern detection latency.

### 2.1 Template Matching

Informally, as Fig. 1 shows, template matching involves sliding the incoming neuronal activity stream over a spatiotemporal template of activity indicators — a matrix corresponding to pre-recorded neural activity where rows correspond to neurons and columns to indicators over a period of time — to determine when there is a sufficient correlation. For clarity, let’s assume that there is only one template. The process proceeds in parallel for multiple patterns.

Formally, the template matching unit accepts as input: i)  $N$  digital streams of spike indicators  $q_n[t] : n \in \{1 \dots N\}$ , each being a single bit denoting if a spike from neuron  $n$  occurred at time  $t$ , and ii) a template matrix  $D \in \mathbb{B}^{N \times M}$  of  $N$  rows and  $M$  columns containing pre-recorded binary indicators over a time period  $M$ . The typical sampling rate for input indicators is 30KHz [26, 30, 56]. However,

the spiking rate of neurons is typically between 1Hz and 20Hz with a 1KHz maximum [45]. Using a much higher sampling rate of 30KHz provides precise temporal resolution for *when* spikes occur. As the indicator stream is noisy, every  $B$  indicators per neuron in the incoming stream and the template are “binned”, that is aggregated into a fixed point value of  $B_{Eff} \ll B$  bits (defined in Subsection 3.4). Binning occurs at runtime for the incoming stream, and off-line for the template  $D$ .  $B$  is chosen empirically to best match the resolution needed. The lower the  $B$  the higher the resolution of the observable spatiotemporal relationships, but also the noisier they become. The matching unit performs correlation once it receives  $M$  indicators. The correlation process is repeated in a sliding window fashion over the input stream, and every time another complete bin of  $B$  indicators per neuron is received. Fig. 2 is an example of binning the incoming stream.

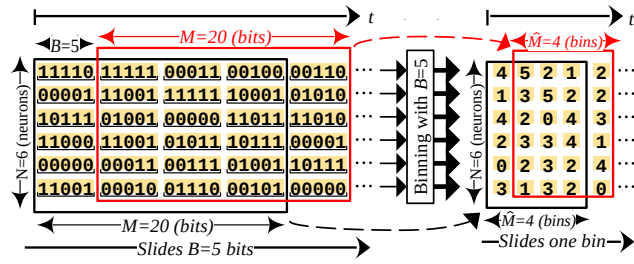


**Figure 2: A toy example of the binning operation over a sliding-window on incoming indicator streams. The  $N \times M$  window slides by  $B = 5$  bits every timestep. Two windows are outlined in black and red.**

Template matching uses the Pearson’s Correlation Coefficient (PCC) which is a general measure of similarity between two samples  $X$ , and  $Y$  of size  $L$  defined as:

$$r(X, Y) = \frac{\sum_{i=1}^L (x_i - \bar{x})(y_i - \bar{y})}{\sqrt{\sum_{i=1}^L (x_i - \bar{x})^2} \sqrt{\sum_{i=1}^L (y_i - \bar{y})^2}}, \quad (1)$$

where  $\bar{x}$  is the arithmetic mean of the sample  $\bar{x} = \frac{1}{L} \sum_{i=1}^L x_i$ .

In template matching we perform the above correlation element-wise between two *binned* indicator matrices: the pattern matrix  $D$  and of an equally sized window  $W$  of the incoming indicator stream matrix  $Q$ .  $D$  and  $W$  are derived from  $N \times M \times B$  indicators, and after binning contain  $N \times \hat{M}$  elements each of  $\lg(B_{Eff})$  bits. The computational and memory needs of PCC vary greatly depending on the following four parameters:  $N$  the number of neurons, the event duration  $M$ , the resolution at which activity is to be aggregated or bin size  $B$ , and finally the number of templates  $T$ .

## 2.2 Multiplexing of the Indicator Streams

While thus far we assumed (for clarity) that there are  $N$  separate incoming streams, one per neuron, the costly analog front-end unit that generates the indicators is typically shared over multiple, if not all neurons [1, 47, 82]. As a result the analog front-end’s output naturally time-multiplexes the indicators of several neurons

over the same digital output serial link as Fig. 3 shows. Given the relatively low acquisition rate of 30KHz per neuron a single digital serial link can easily communicate the indicators of 10s of thousands of neurons. Without loss of generality, from this point on we assume that all  $N$  neurons are serialized into a single batch of  $N$  binary indicators all corresponding to the same time step.  $B$  of those batches are read to form a complete bin, thus  $NB$  serial indicators are read as a complete bin. Similarly,  $\hat{M}$  bins are read to form a complete sliding window, thus  $N\hat{M}B$  serial indicators are read as a complete sliding window.

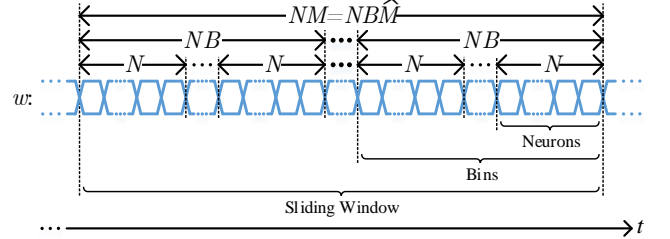


**Figure 3: The indicators from multiple neurons are time-multiplexed over a single serial link.**

## 2.3 Implementation Challenges

Table 1 identifies four configurations that are representative of current and future applications as per the following best-practices in neuroscience: In accordance with previous neuroscience research demands and configurations, bin sizes range from 5 to 250msec [23, 46, 62, 74, 81] while window values range from 1 to 9sec [74]. The maximum number of neurons recorded with electrophysiology is around 3000 [72], while the number of templates may vary (and can be increased) as the use-cases demand. Accordingly, for the purpose of stress-testing, our configurations ( $CFG_{1-4}$ ) encompass the extreme values currently used in neuroscience ( $CFG_1$ ) while anticipating an increase in the number of neurons simultaneously recorded as technology evolves ( $CFG_4$ ). For applications that involve detecting memories (e.g., traumatic events), templates of 5 to 9 seconds ( $M$ ) binned over 5 to 250 msec ( $B$ ) are of interest (recall, the acquisition rate is 30KHz).

**Table 1: Representative Hyperparameter Configurations and resulting GOPS/Template and Memory Footprints.**

	$N$	$T$	$M$		$B$		Requirements		
	Neurons	Templates	Samples	sec.	Bins	Samples	nsec.	GOPS/Template	Memory (Mb)
$CFG_1$	1K	1	150k	5	20	7500	250	0.6	0.3
$CFG_2$	10K	2	150k	5	1000	150	5	314.0	114.4
$CFG_3$	20K	3	270k	9	36	7500	250	21.6	33.0
$CFG_4$	30K	4	270k	9	1800	150	5	1696.6	1236.0

The table also reports: a) the number of arithmetic operations needed over a single template and one window of the input, and b) the on-chip memory needed. The sheer volume of data and number of computations can be daunting especially for untethered

applications. In real-time applications, another major challenge emerges: the bulk of the computations can be performed only after the last indicator has been received, exacerbating computation and memory needs. The hardware has to be capable of performing the computations within stringent latency constraints, and also has to buffer a window sized sample of the binned input streams which further increases memory demands. Another undesirable feature of PCC is that the bulk of the computations have to use floating point arithmetic. Coupled with the latency constraints this necessitates numerous, expensive execution units. Section 5 presents an optimized vector-unit-based that implements Pearson's Correlation Coefficient as originally proposed and currently used.

### 3 NOEMA

This section presents *Noema* which overcomes the challenges of exiting PCC implementations. Central to *Noema* is a novel decomposition of the PCC into simple bit-level operations which Subsection 3.1 presents. Subsection 3.2 and Subsection 3.3 detail the hardware implementation. Subsection 3.4 discusses the on-chip memory required motivating the hardware efficient template encoding method presented in Subsection 3.5. Finally, Subsection 3.6 explains scaling in the number of neurons and templates.

#### 3.1 Reformulating Pearson's Correlation

Recall that the PCC between two samples  $X$  and  $Y$  of length  $L$  is defined in Equation (1). Substituting the arithmetic means, squaring and rearranging the PCC equation yields:

$$r(X, Y)^2 = \frac{\left( L \sum_{i=1}^L x_i y_i - \sum_{i=1}^L x_i \sum_{i=1}^L y_i \right)^2}{\left( L \sum_{i=1}^L x_i^2 - \left( \sum_{i=1}^L x_i \right)^2 \right) \left( L \sum_{i=1}^L y_i^2 - \left( \sum_{i=1}^L y_i \right)^2 \right)} \quad (2)$$

Let  $D$  (template) and  $W[t]$  (input indicator stream window starting at time  $t$ ) be respectively two matrices of indicators. Our goal is to calculate the PCC of the *binned*  $\widehat{D}$  and  $\widehat{W}[t]$ . Recall that before binning  $D$  and  $W$  contain  $N \times \widehat{M} \times B$  indicators, whereas  $\widehat{D}$  and  $\widehat{W}[t]$  contain  $N \times \widehat{M}$  binned values where  $\widehat{M} = M/B$ ,  $B$  the number of indicators per bin,  $N$  the total number of neurons, and  $M$  the per neuron sample count in indicators of the template. Let  $d_{n,c,b}$  and  $\widehat{d}_{n,\widehat{c}}$  be respectively the indicators and the corresponding binned indicators of the template  $D$  and where  $n$  a neuron,  $c$  and  $\widehat{c}$  respectively columns of the pre-binned  $D$  and the binned  $\widehat{D}$ , and  $b$  the 3rd dimension index of the indicator matrix  $D$  that are binned together to produce the binned values of  $\widehat{D}$ . Similarly,  $w_{n,c,b}[t]$  ( $\widehat{w}_{n,\widehat{c}}[t]$ ) refer to the corresponding elements for the current window  $W[t]$  ( $\widehat{W}[t]$ ) matrix captured from the incoming stream.

We observe that the squared Pearson's Correlation Coefficient can be split into constants and summations:

$$r[t]^2 = \frac{(C_1 S_1[t] - C_2 S_2[t])^2}{C_3 (C_1 S_3[t] - S_2[t]^2)}, \quad (3)$$

where the constants are – recall, all  $\widehat{d}_{x,y}$  are statically-known binned template values:

$$C_1 = \widehat{M}N, \quad C_2 = \sum_{\widehat{m}=1}^{\widehat{M}} \sum_{n=1}^N \widehat{d}_{n,\widehat{m}}, \quad C_3 = C_1 \sum_{\widehat{m}=1}^{\widehat{M}} \sum_{n=1}^N \widehat{d}_{n,\widehat{m}}^2 - C_2^2, \quad (4)$$

and the summations are:

$$\begin{aligned} S_1[t] &= \sum_{\widehat{m}=1}^{\widehat{M}} \sum_{n=1}^N \widehat{w}_{n,\widehat{m}}[t] \widehat{d}_{n,\widehat{m}} \quad (\text{element-wise multiply-sum}) \\ S_2[t] &= \sum_{\widehat{m}=1}^{\widehat{M}} \sum_{n=1}^N \widehat{w}_{n,\widehat{m}}[t] \quad (\text{accumulation}) \\ S_3[t] &= \sum_{\widehat{m}=1}^{\widehat{M}} \sum_{n=1}^N \widehat{w}_{n,\widehat{m}}[t]^2 \quad (\text{sum of squares}). \end{aligned} \quad (5)$$

The constants, hereafter referred to as Pearson's constants, are terms involving templates only (independent of the sliding indicator matrix  $\widehat{W}[t]$ ) and can be computed offline. The summations, hereafter referred to as Pearson's summations, are terms dependent on  $\widehat{W}[t]$  and can only be calculated at runtime, once a complete bin is received. We next detail our efficient computation of Pearson's summations based on bit-serial binary indicator arithmetic.

#### 3.2 Implementing the Pearson's Sums

**Summation  $S_2$**  is the sum of all binned values in the incoming window. Since each binned value is itself a count of indicators,  $S_2$  is simply the count of *all*  $NM$  indicators in the window. While this count changes as the window slides, we avoid storing the whole window. As described in Algorithm 1, we store the population count per column (bin) of the sliding matrix  $\widehat{W}[t]$  into memory  $R_2$  (line 6). Once we complete the accumulation of a new column  $P_2$  that enters to the sliding window (line 5), we add this column sum to the final  $S_2$  sum and subtract the column that exits the sliding window and was computed  $\widehat{M}$  columns in the past (line 7).

---

##### Algorithm 1: $S_2$ Summation Process.

---

```

// all variables are initially zero
1 while TRUE do
2   for  $\widehat{m} = 1$  to  $\widehat{M}$  do
3     for  $b = 1$  to  $B$  do
4       for  $n = 1$  to  $N$  do
5         // timestep:  $(\widehat{m} - 1)BN + (b - 1)N + n$ 
6         // if  $w$  indicates a spike
7         // Increment column sum
8          $P_2 \leftarrow P_2 + w$ ;
9
10        // store current column sum to  $R_2$  RAM
11         $R_2[\widehat{m}_p] \leftarrow P_2$ ;
12        // add newestColumn-oldestColumn to  $S_2$ 
13         $S_2 \leftarrow S_2 + P_2 - R_2[\widehat{m}];$ 
14        Send a copy of current  $S_2$  to next stage;
15         $P_2 \leftarrow w$ ; // clear column sum
16         $\widehat{m}_p \leftarrow \widehat{m}$ ; // store previous  $\widehat{m}$ 

```

---

Fig. 4 (c) shows the hardware implementation of  $S_2$  PE. First, we accumulate the input indicators (received serially at  $w$ ) into the  $S_2$  column sum register ( $P_2$ ). The control signal  $sEnb$  indicates when a column sum is ready. This happens every  $N\widehat{M}$  cycles. Once we finish accumulating a column (bin) of indicators, we move the sum  $P_2$  to the column sum memory  $R_2$  and reset  $P_2$  to prepare it for the next column accumulation. The final stage of processing  $S_2$  is the bit-serial add-sub-accumulate. This block receives the new column sum (to be added) from the column sum register  $P_2$ , and the oldest column sum (to be subtracted) from the column sum

memory  $R_2[\widehat{m}]$ . Both of these sums are serialized using a Parallel-Input-Serial-Output (PISO) unit, and the difference of those sums is accumulated (serially) to the final  $S_2$  value.

**Summation  $S_3$** , as shown in Equation (5) requires accumulating the squares of the binned input. One approach is to accumulate the binned indicators and then square the accumulated value for each bin. This is expensive as it has to accumulate values ahead of processing, and a cost-prohibitive squarer circuit for each bin of a total of  $N$  bins. Instead, we break the squares into partial sums that will be generated and accumulated as new values are received by utilizing the popular sum of first odd natural numbers equation:

$$a^2 = \sum_{i=1}^a (2i - 1). \quad (6)$$

Substituting in Equation (5) yields:

$$S_3[t] = \sum_{\widehat{m}=1}^{\widehat{M}} \sum_{n=1}^N \widehat{w}_{n,\widehat{m}}[t]^2 = \sum_{\widehat{m}=1}^{\widehat{M}} \sum_{n=1}^N \sum_{i=1}^a (2i - 1) \quad (7)$$

Where the upper bound for  $a$  is  $\widehat{w}_{n,\widehat{m}}[t]$ , the corresponding binned value. This summation happens on-the-fly, incrementing  $a$  every time a 1 is received. Accordingly, we do not need to know the upper bound in advance. We “discover” it naturally as the stream is received.

For efficient implementation, the summations should be organized to match the order in which the indicators are received as shown in Fig. 3:  $\widehat{m}$  in the outer summation,  $b$  in the middle summation, and  $n$  in the inner summation, namely  $\sum_{\widehat{w}=1}^{\widehat{M}} \sum_{b=1}^B \sum_{n=1}^N$ . For this purpose, we need to keep the running indexes  $i$  for each element of the current column. This can be solved by storing intermediate copies of the variable  $i$  one per neuron  $n$ , as described in Algorithm 2.

Algorithm 2 is very similar to Algorithm 1, however, we store a copy of the current index  $i$  of neuron  $n$  into the memory location  $i_n$ .  $i_n$  is incremented if the spike indicator  $w$  is active, and will be cleared for every  $n$  on the first bit of each the bin (line 5). The column sum  $P_3$  will be incremented by  $2i_n - 1$  if the incoming indicator  $w$  is active. This will generate the sum of squares as dictated by Equation (6).

As illustrated in Fig. 4 (b), we accumulate the incoming indicators into an *indices memory* for each neuron of the  $N$  neurons separately, say  $i_n$  for neuron  $n \in \{1, \dots, N\}$ . Afterwards we compute  $2i_n - 1$ , and accumulate it to the column sum register  $P_3$ . The computation of  $2i_n - 1$  is performed for each neuron separately. The control signal  $iRst$  is activated every  $B$  cycles for a period of  $N$  cycle to clear the previous content of the memory. Note that we start accumulating the fragments of the squares before having the complete square value. The rest of  $S_3$  PE is similar to  $S_2$  PE.

**Summation  $S_1$** , as shown in Equation (5), is different than the previous two sums as it involves the template.  $S_1$  is an element-wise multiply-sum of elements from the binned template and elements from the sliding spikes matrix. The major challenge of element-wise multiply-sum that it requires recomputing all matrix elements for each incoming bin (a column in the matrices). Unlike  $S_2$  and  $S_3$  we cannot perform this summation by adding the difference between the first and the last column. However, our approach simplifies this compute-intensive operation and does not require any multiplier.

---

### Algorithm 2: $S_3$ Summation Process.

---

```

// all variables are initially zero
1 while TRUE do
2   for  $\widehat{m} = 1$  to  $\widehat{M}$  do
3     for  $b = 1$  to  $B$  do
4       for  $n = 1$  to  $N$  do
5         // timestep:  $(\widehat{m}-1)BN + (b-1)N + n$ 
6         // if first bit in bin clear sum index,
           otherwise increment
            $i_n \leftarrow w + \begin{cases} 0 & \text{if } b = 1, \\ i_n & \text{otherwise;} \end{cases}$ 
           // if  $w$  indicates a spike
           // increment sum index
            $P_3 \leftarrow P_3 + w(2i_n - 1);$ 
7         // store current column sum to  $R_3$  RAM
            $R_3[\widehat{m}_p] \leftarrow P_3;$ 
           // add newestColumn-oldestColumn to  $S_3$ 
            $S_3 \leftarrow S_3 + P_3 - R_3[\widehat{m}];$ 
           Send a copy of current  $S_3$  to next stage;
10         $P_3 \leftarrow w;$  // clear column sum
11         $\widehat{m}_p \leftarrow \widehat{m};$  // store previous  $\widehat{m}$ 

```

---

We instead use an accumulator for each of the matrix columns by substituting the binned form of the input spikes sliding matrix  $\widehat{Z}$  from Equation (5) with the serialized input  $w$ .  $S_1$  will thereby be computed by:

$$S_1[t] = \sum_{\widehat{m}=1}^{\widehat{M}} \sum_{n=1}^N \sum_{b=1}^B \begin{cases} \widehat{d}_{n,\widehat{m}} & \text{if } w_{n,\widehat{m},b}[t] = 1 \\ 0 & \text{otherwise} \end{cases} \quad (8)$$

For each of the  $N$  neurons, the binned value of the template is accumulated if the input spike indicator  $w$  is active. For instance, if the incoming spike indicators stream is “...0100101” and the current bin value is  $x$ , the value of  $x$  will be accumulated three times. The accumulators are connected in series to implement the sliding window. Once a complete bin (column) is computed (i.e., control signal  $sEnb$  is asserted), its accumulated value is moved and accumulated in the neighboring accumulator. After  $\widehat{M}$  successive bin accumulations, all  $\widehat{M}$  bins (columns) will be accumulated in the leftmost register. Finally, the accumulated  $S_1$  is serialized.

### 3.3 Post-Processing

To find the Pearson’s Correlation Coefficient value, we substitute the Pearson’s sums together with the pre-computed Pearson’s constants into Equation (3). This computation requires (1) a constant multiplier, (2) a subtractor, (3) a squarer, and (4) a fractional divider. To reduce the overhead of the post-processing hardware, it has been implemented using traditional bit-serial arithmetic. Fig. 5 illustrates a family of bit-serial arithmetic circuits that were modified to fit our needs. Our implementation exhibits a unit latency, namely, the first output bit is generated at the same cycle that the first valid bit has been received. Simply, the first valid bit propagates through a combinatorial logic to generate the first valid bit. A single register is added between each cascaded unit to break long combinatorial paths that may be created. The constant multiplier and squarer are modified versions of Gnanasekaran’s carry-save add-shift semi-systolic multiplier [27]. While the aforementioned bit-serial arithmetic circuits require a control signal to indicate the last bit of bit-serial value, our modifications are only required to

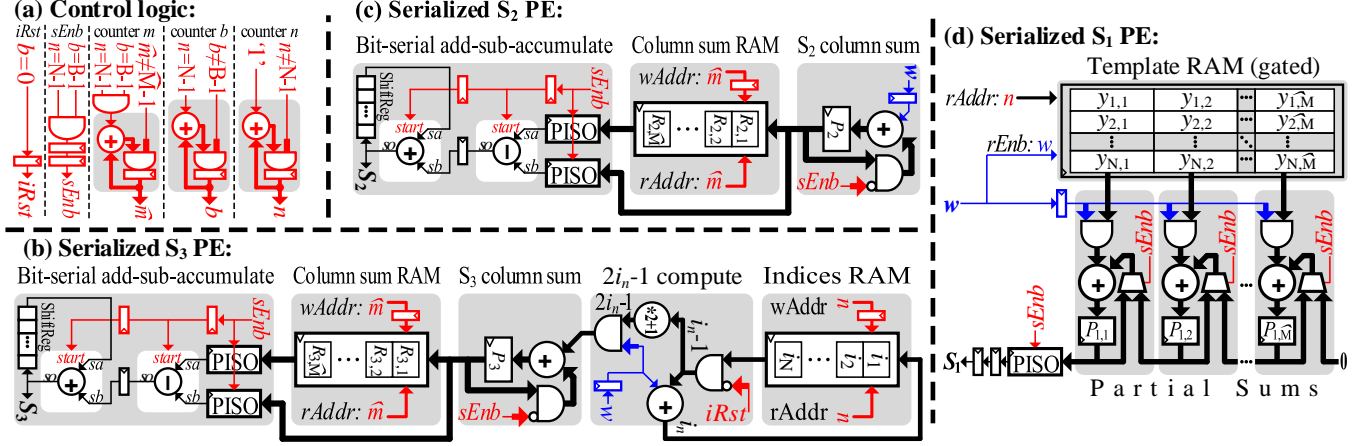


**Figure 4: OURL's core compute units. (a) control logic. (b) Sum of sample squares  $S_3$ . (c) Sample sum  $S_2$ . (d) Element-wise sample-template multiply-sum  $S_1$ .**

indicate the first bit of the bit-serial value at the beginning of the computation. This further simplifies the design. An ultra low-area fractional divider has also been implemented.

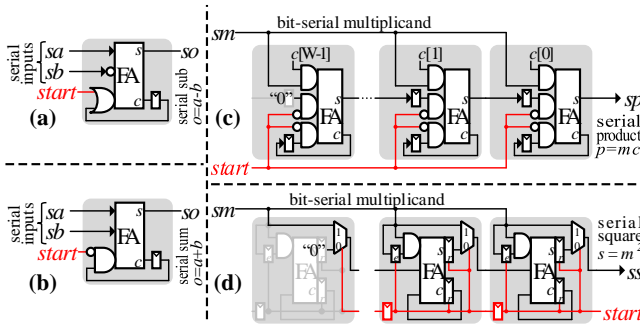


**Figure 5: Bit-level arithmetic units: (a): Adder. (b): Subtractor. (c) Constant multiplier. (d): Squarer.**

Fig. 6 (b) shows the implementation of the post-processing circuitry. The post-processing unit receives bit-serial Pearson's sums, and bit-parallel Pearson's constants. Our bit-serial arithmetic units are cascaded to compute the squared PCC as formulated in Equation (3). To increase the maximum possible  $F_{\max}$ , we pipeline the computation together with the *start* signals that synchronize the computation start time for each unit. The computation performance and latency are dominated by the fractional divider, thus the post-processing units can process one set of inputs every  $WP$  cycles, where  $W$  is the data width and  $P$  is the precision of the output.

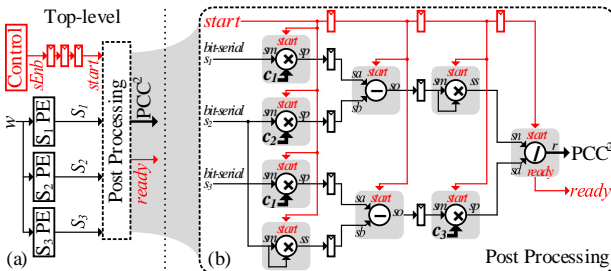


**Figure 6: Template matching system: (a) Top-level hierarchy. (b): Post-processing unit.**

The post-processing unit has two major inputs, the Pearson's sums and the Pearson's constant. The Pearson's sums are generated serially by  $S_1$  PE,  $S_2$  PE, and  $S_3$  PE. As depicted in Fig. 6, the post-processing unit receives those sums as bit-serial inputs, together with a control signal to start the processing. On the other hand, Pearson's constants are generated offline and are loaded to the post-processing unit.

### 3.4 On-Chip Memory Costs

Table 2 shows the cost in *bits* of the various storage elements given a configuration.  $B_{eff}$  is the expected maximum count for the bin values. This maximum is a function of the intrinsic firing rate of the brain and of the sampling rate used by the analog front-end. It is known that the neurons fire at a maximum rate of 1KHz, whereas a commonly used sampling rate for neuroprobes is 30KHz (e.g. Intan technologies data acquisition system). The higher sampling rate permits a resolution that is necessary for identifying *when* spikes occurs. Accordingly, the expected maximum value for a binned value will not exceed  $B/30$ , where  $B$  is the total number of samples binned per value. A real example, confirmed using indicator traces from mice [71], demonstrated that for  $B = 150$  the maximum expected value  $B_{eff} = 5$ . As Subsection 5.1 will show, most of *Noema's* area is consumed by the template memory. Accordingly, we consider space efficient encoding of the template matrix next.

**Table 2: Storage usage in bits.**

Sub-module	Resource	Width	Depth
$S_1$ PE	Registers ( $P_1$ , PISO)	$\widehat{M} \log_2(N\widehat{M}B_{eff}^2)$	1
	Template RAM	$\widehat{M} \log_2(B_{eff})$	$N$
$S_2$ PE	Registers ( $P_2$ , PISO, SR)	$\log_2(N^4\widehat{M}B_{eff}^4)$	1
	Column RAM ( $R_2$ )	$\log_2(NB_{eff})$	$\widehat{M}$
$S_3$ PE	Registers ( $P_3$ , PISO, SR)	$\log_2(N^4\widehat{M}B_{eff}^8)$	1
	Column RAM ( $R_3$ )	$\log_2(NB_{eff}^2)$	$\widehat{M}$
	Indices RAM ( $i$ )	$\log_2(B_{eff})$	$N$
Post-Processing	Registers	$80 \log_2(N\widehat{M}B_{eff})$	1

### 3.5 Template Memory Compression

As Table 3 shows, the template memory size can reach hundreds of Mbits. While feasible, such memory sizes are undesirable for untethered applications. Using off-chip memory is also undesirable due to its energy and latency costs compared to using on-chip SRAM. Therefore, we explore the alternative of compressing template values on-chip.

We find that templates collected from thousands of neurons in mice [71] exhibit a geometric distribution of values, where low magnitude values dominate. Accordingly for the case of  $B = 150$  (max binned value  $B_{Eff} = 5$ ) we encode the values 0, through 5 respectively as  $0b$ ,  $10b$ ,  $110b$ ,  $1110b$  and  $1111b$ . However, for larger values of  $B$  unary decoding requires large one-hot to binary decoders. Inspired by Golomb[28] and Rice[63] codes, we mix unary and binary codes to implement a simple-to-decode variable length encoding scheme referred to as  $UB_{u,b}$  coding. A  $UB_{u,b}$  code represents a UB code with unary variable-length codes of maximum  $u$ -bits length, and a binary fixed-length code of  $b$ -bits length. For example, for  $B = 7500$  (max binned value  $B_{Eff} = 250$ ) we use a  $UB_{4,8}$  encoding. That is, values up to 3 are encoded in unary, whereas larger values are encoded with a prefix of  $1111b$  followed by the actual value  $v$ . This encoding uses 12b in total for all values above 3. There are many other possible encoding methods that are worthwhile exploring. However, they would need to carefully balance the area, complexity, energy, and compression ratio. This is left for future work.

Fig. 7a illustrates our implementation for an example  $UB_{4,5}$  for clarity. To allow a single code decoding per cycle, we arrange the compression data in lines of  $u + b = 4 + 5$  bits width. We read a single line every cycle and store the previously read line to allow processing the remaining bits from the previous line. The previous line and the current line are packed as a double-width line. The core of the decompression engine is a barrel shifter that allows reading the data from a specific starting position. After shifting the data, we know that the first  $u + b$  bits are the current code. The first  $u$ -bits are the unary part and are processed using a  $u$ -bits priority encoder to receive the index of leading zero. If all  $u$ -bits are 1's, the current code is binary; we read the next  $b$ -bits from the binary code portion then add  $u$  to generate the decompressed data. Otherwise, the current code is unary; the output of the priority encoder (index of leading zero) is actually the decompressed data. The rest of the circuitry computes the starting index of the next code and the generates the enable signal that enables reading the next line from the memory once the remainder of the combined current and previous lines is less than  $u + b$  bits. We use one decompressor unit per template memory column.

### 3.6 Scaling

**Templates:** Fig. 7b shows how it can scale to support multiple templates. Fortunately, sums  $S_2$  and  $S_3$  are functions of the input stream solely. Accordingly, we need to replicate only the  $S_1$  and the post processing units.

**Neurons:** The first parameter available to scale up the number of neurons that *Noema* can process is its operating frequency. Since the units perform their computation at the same rate as the data is received, the frequency needs to be  $N \times KHz$  for the design as shown to process  $N$ . To surpass the limitations of the frequency. we can

scale to even more neurons by partitioning the input stream coupled with replication of the compute components as Fig. 7c shows. The example shows scaling up to  $4 \times$  more neurons by partitioning the input stream into four sub-streams, where each sub-stream is assigned its own set of sum units. The post processing unit is scaled up accordingly. The costs would be linear for the replicated sum units, whereas they are logarithmic for the post-processing unit. Fortunately, we can also simply partition the template memory, as with the input neurons. The overall area of the template memory will be mostly unaffected by the required partitioning. As the evaluation section shows, the relative cost of the processing logic in *Noema* is negligible compared to the template memory.

**Tuning Frequency and Power:** We can further reduce frequency and improve power efficiency by purposely partitioning the input stream while using more processing units. The low area needed by the compute portion of the design makes this an effective approach. Of course, care must be taken to ensure that latency remains within real-time limits. Fortunately, for the most demanding configuration we studied, the latency for producing the correlation output per window is only 700 cycles where even at a reduced clock frequency of 140KHz, *Noema* would still meet the 5ms requirement. Finally, by delaying the incoming stream  $w$  in Fig. 4 by one cycle, *Noema* avoids accessing the template memory when the indicator is 0. This improves energy consumption by nearly 7X for the most demanding configuration studied as the indicator stream is sparse.

## 4 RELATED WORK

There has been no prior work on hardware accelerated PCC for processing neuronal signals for pattern matching in real time. Small scale prototype implementations of PCC routinely use commodity platforms and are computed offline. The development and implementation of new algorithms for neural decoding has been continuously expanding since 2002, when a monkey was able to move a computer cursor, directed from neural signals alone [65]. While motor prosthetics often use Kalman filters in real time, and combine them with of PCC template matching to identify events corresponding to motor memory. [21]. Accordingly, various algorithmic approaches need to be tailored to particular brain regions and the type of brain activity being detected.

In general, prior techniques for accelerating PCC can be classified along two axes. The first is the type of platform used, (1) CPUs [67], (2) GPUs [22, 38, 44], and (3) hardware-oriented techniques on FPGAs [61]. The second is the target application, where the only work on PCC acceleration has been directed at offline analysis of connectivity maps based on fMRI (blood flow) image data [61]. Thus methods for acceleration of high-resolution (i.e. neuronal signal) pattern matching remains to be investigated. Previous research on template matching in populations of neurons with the Pearson's Correlation Coefficient [23, 46, 62, 74, 75, 79, 81] has been performed with PCC and executed on commodity CPUs and GPUs operating offline, with no explicit latency constraints or focus on acceleration. Data parallelism within and across windows and batching across multiple input traces are used to maximize throughput. For real-time applications, and as Subsection 5.4 confirms, optimized GPU implementations can meet latency constraints only for the less demanding configurations necessitating energy and latency optimized solutions such as *Noema*.



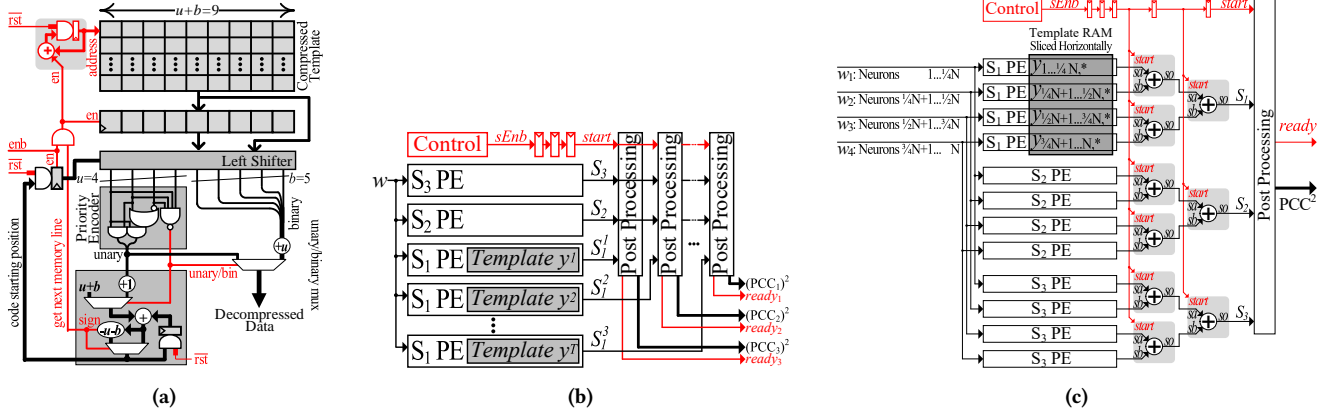


Figure 7: (a) Example UB<sub>4,5</sub> decompression circuit. Scaling: (b) template count  $T$ , and (c) neurons  $N$ .

## 5 EVALUATION

**Experimental Setup and Framework:** We use actual neuron indicator streams collected over 2400 seconds from 6446 neurons of three mice, *Waksman*, *Robbins*, and *Krebs* [71]. For experiments requiring inputs from more neurons, we augment these traces by sampling per neuron activity from the existing trace while maintaining the overall activity factor. We perform synthesis and layout of all designs using Synopsys’ Design Compiler [73] with a TSMC 65nm technology library. We constrain the target frequency to be only as high as necessary to meet the timing requirements of each specific configuration. Layout placement and routing is performed using Cadence Innovus [14], and we estimate the power consumption in Innovus using the post-layout netlist with an activity factor of  $F_{f,avg}/F_s = 1/1500$ . This is the ratio between the average neuron firing rate and the sampling rate, which represents the typical neural activity factor as validated by the input datasets we use. The area and power estimation of the on-chip SRAM blocks were modeled in CACTI [31].

**Optimized Baseline Implementation:** Given the data parallelism, and the specific computation and dataflow patterns of PCC, we also consider  $PCC_{BASE}$  as an alternate to *Noema*.  $PCC_{BASE}$  computes the Pearson’s Correlation Coefficient on binned values as it was originally proposed and implemented in highly optimized GPU implementations.  $PCC_{BASE}$  utilizes a vector-unit-based architecture where the units have been carefully customized in count and type to perform only the various computations PCC needs and to localize communication.  $PCC_{BASE}$ ’s memory and datapath were customized to scale to the more realistic configurations avoiding centralized memory blocks, off-chip accesses and long data busses for maximum energy efficiency. We also equip  $PCC_{BASE}$  with the same template compression method as *Noema*.

As Fig. 8 shows, a *Binning* unit converts the serialized input  $w$  into the corresponding bin values per neuron. After  $NB$  cycles, the binning memory will include the value of the current bin for all  $N$  neurons. As the last  $N$  indicators are received, the bin values are finalized one per neuron per cycle. At that time, they are transferred one by one to the corresponding column in the sliding matrix unit. The sliding matrix unit contains  $N\hat{M}$  elements each of  $lg(B_{eff})$  bits. Each  $NB$  cycles we choose the next column of sliding matrix and write to the corresponding segment. This will implement a sliding window of the binned spike indicators.

A set of vector processing elements (VPEs) perform the bulk of the computations needed by the correlation. For this purpose we split the correlation computation into components that can be performed over binned columns of the input (intra-column operations), and a final step that combines the per column operations to produce the final output (cross-column). The intra-column operations are computed by the VPEs. A Scalar processing element (SPE) performs the cross-column computations. Rather than allocating a VPE per template column, we split the sliding matrix column-wise into  $p$  columns where  $p$  is tuned to achieve the required acceleration.

A template unit contains  $T$  templates which it matches against the incoming stream. There are  $NMT$  elements in the template unit each having  $lg(B_{eff})$  bits. For our evaluation we use the template encoding method of Subsection 3.5 which is directly compatible with this design also. Each column of the template matrix is thereby  $N\hat{M}T/p$ .

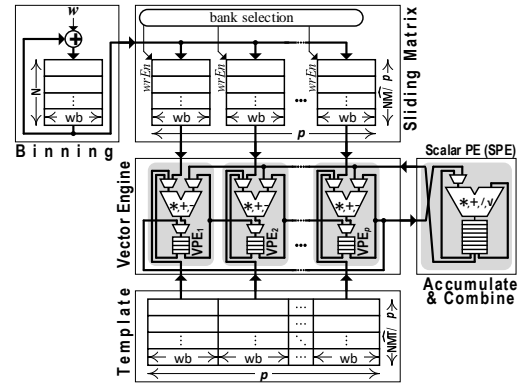


Figure 8: A bit-parallel pattern matching baseline model. Control signals are omitted for clarity.  $wb = lg(B_{eff})$

The VPEs and the SPE contain each  $4 \times 32b$  register files for storing their intermediate results reducing overall energy vs. using a common register file across multiple lanes. The VPE register-files are chained together to form a shift-register. This allows accumulating column data and to move the data for processing by the SPE. As a result, we have  $NB$  cycles to process the sliding matrix and to generate the PCC before the next binned column arrives and contaminates the sliding matrix content. The VPEs and the

SPE implement floating-point arithmetic, as all operations with the incoming binned data as per Equation (1) entail an average. For the most demanding configuration  $CFG_4$  single-precision is needed as the individual sums in Equation (1) involve the accumulation and multiplication of  $30,000 \times 18,000$  8b inputs.

We configure the number of lanes  $p$  to the minimum required to meet the 5msec latency requirement. Considering the latency in cycles per stage, we arrive at the following constraint (derivation omitted due to space limitations):

$$5T\left(\frac{2N\hat{M}}{p} + p\right)/F_{\max} < \min\left(\frac{B}{30000}, 0.005\right). \quad (9)$$

An implementation using a TSMC 65nm process and Synopsys optimized FP32 units achieves a maximum frequency of  $F_{\max} = 270MHz$ . Accordingly for the evaluation configurations  $CFG_{1..4}$  from Table 1, the number of lanes used  $p$  is 1, 201, 22, and 2,263, respectively.

The data range and hence datatype needs for accurate PCC calculation depend on configuration and input data distribution which in turns depend on the complexity of the spike-sorting front-end chosen and the subject/application. Our experiments show that the baseline architecture based on Equation (1) should use a single-precision FP format to avoid loss of accuracy due to accumulator saturation. Were baseline to implement the modified PCC equation Equation (2), int32 or higher could be used since the arithmetic means of the samples are not required. The scalar PE would need to still be in FP32. Compared to using a single-precision FP format to compute Equation (1), using int32 reduces the area of the vector engine by 37% and its power 43%. Taking the most intensive configuration  $CFG_4$ , for example, the int32 baseline would use 12× more power, that is an order of magnitude more power than *Noema* for two reasons (see Subsection 5.2): a) the power used by the *Noema* PEs is 6.6× less, and b) the baseline’s template memory and buffers dominate power consuming 15.5× more than that of *Noema*. In our baseline architecture we use a floating-point format since unlike integers, it won’t fail for higher problem dimensions avoiding the introduction of additional complexity in applications.

## 5.1 On-Chip Memory

Template memory dominates area for the higher-end configurations. Recall, that without template compression, the capacity needed is a function of  $\hat{M}$ ,  $N$ , and  $B_{Eff}$ . As this section shows however, compression can greatly reduce template footprints and thus the on-chip memory needed. Accordingly, before we can evaluate the ASIC and FPGA implementations, we first determine the size of the on-chip Subsection 5.1 template memory each configuration would need.

**Table 3: Register and On-Chip Memory Configurations after Template Compression.**

	<i>Noema</i>								<i>PCCBASE</i>		
	S1 PE		S2 PE		S3 PE		PP	Slicing RAM (Mb)	Template RAM		
	Reg (Kb)	Tmpl RAM (Mb)	Reg (b)	Col. RAM (Kb)	Reg (b)	Col. RAM (Kb)	Idx. RAM (Kb)		Uncompressed (Mb)	Compressed (Mb)	
CFG1	0.6	0.08	77	0.35	108	0.51	7.81	1.7	0.15	0.15	0.08
CFG2	27.3	31.10	73	15.63	82	17.58	29.30	2.0	57.22	57.22	31.10
CFG3	1.3	5.89	95	0.81	127	1.09	156.25	2.2	16.48	16.48	5.89
CFG4	53.3	220.70	80	31.64	89	35.16	87.89	2.2	617.98	617.98	220.70

**Table 4: Throughput and Latency of *Noema* and *PCCBASE*.**

CFG	Throughput (PCC/sec)				Detection Latency (msec)			
	1	2	3	4	1	2	3	4
<i>PCCBASE</i>	4	400	12	800	0.74	4.98	4.71	5.00
<i>Noema</i>	4	400	12	800	0.0239	0.0028	0.0015	0.001

Fig. 9 reports the memory footprint for the four configurations of Table 1 and different templates with and without template compression. All footprints are normalized to the footprint of the uncompressed template per configuration. We show results for three different templates per input sample trace; a *worst case* which is the frame from the neuron recording with the least sparsity, and two templates which are randomly selected windows. The worst case template dictates the compression ratio used to size the on-chip template memory.



**Figure 9: Normalized template memory footprints.**

As expected, uncompressed footprint templates vary considerably, from 150Kb for  $CFG_1$  to more than 600Mb for  $CFG_4$ . Our lightweight lossless compression method is effective in reducing footprints, and more so where it matters the most. That is for  $CFG_2$  ( $B = 150$ ,  $\hat{M} = 1000$ ) and  $CFG_4$  ( $B = 150$ ,  $\hat{M} = 1800$ ) configurations where footprints are reduced by at least 2.79× for all templates. We size our on-chip memories for the worst case across the three templates per configuration. The resulting template memory sizes are shown in Table 3. The table also reports the number of bits used by the various registers per unit in *Noema* and the total on-chip memory needed by *PCCBASE*. While *PCCBASE* can benefit from template compression for its own template memory, it still needs a window memory for the incoming indicator streams. As we show, the ASIC implementation of *Noema* meets real-time requirements for all configurations and, as expected, requires considerably less power than the FPGA implementation.

## 5.2 Performance, Power, and Area

Table 4 shows the performance of *Noema* and *PCCBASE* in terms of throughput (number of correlations computed per second) and latency (time from arrival of last data bit to complete computation) for the four configurations. All designs are configured to meet the throughput and latency requirements. For  $CFG_2$  through  $CFG_4$  we use three partitions, each processing 1/3 of the neurons as per Subsection 3.6. *Noema* far exceeds the real-time latency requirements, as it requires just 700 cycles to produce its output once the last indicator for a window is received.

Table 5 shows the power usage of *Noema* and *PCCBASE* for the four configurations, including a breakdown in memory and compute. *Noema*’s power is considerably lower than that of *PCCBASE*

**Table 5: Power: Breakdown of power in mW consumed by memory and compute in *Noema* and  $PCC_{BASE}$ .**

	$PCC_{BASE}$			<i>Noema</i>		
	Memory	Compute	Total	Memory	Compute	Total
CFG1	7.87	17.34	25.22	0.30	0.43	0.73
CFG2	1236.74	607.29	1844.03	89.78	84.28	174.06
CFG3	198.94	81.12	280.06	18.55	9.68	28.23
CFG4	10718.07	6550.65	17268.72	682.70	522.76	1205.46

**Table 6: Silicon area in  $mm^2$  for *Noema* and  $PCC_{BASE}$ .**

	$PCC_{BASE}$			<i>Noema</i>		
	Memory	Compute	Total	Memory	Compute	Total
CFG1	0.38	0.15	0.53	0.10	0.02	0.11
CFG2	81.50	5.87	87.37	28.46	1.35	29.81
CFG3	15.60	0.77	16.37	6.26	0.09	6.25
CFG4	469.42	63.48	532.90	202.00	3.42	205.42

for all configurations for three reasons: 1) *Noema* does not need a sliding window memory, 2) the compute units are much more energy efficient, and 3) *Noema* can avoid accessing the template memory when a bit indicator is 0 (most will be 0 due to the nature of brain activity).  $PCC_{BASE}$  can only exploit sparsity of binned values instead. In  $PCC_{BASE}$  compute units are responsible for a significant fraction of overall power for all configurations, This is not the case for *Noema* where memory dominates total power.

Table 6 reports the area in  $mm^2$  for *Noema* and  $PCC_{BASE}$  as configured to meet the real-time requirements of the four configurations. The table also shows a breakdown in the area used for memory and compute component. *Noema* is considerably smaller than  $PCC_{BASE}$ . Since that all designs use our template compression, the savings with *Noema* are due to: 1) eliminating the sliding window memory, and 2) from using much smaller bit-serial compute units. For the  $CFG_4$  configuration, *Noema* is nearly 2.6 $\times$  smaller than  $PCC_{BASE}$ . Using a more recent technology node would significantly reduce overall area. SRAM cells in a 14nm process can be 6 $\times$  to 8 $\times$  smaller compared to 65nm [11, 55, 64, 68].

### 5.3 FPGA Implementation

We implement *Noema* on a Stratix 10 FPGA (1SG280LN2F43E1VG) [4] using Intel’s Quartus compiler [3]. To minimize power, the target frequency is constrained to be only as high as necessary to meet the performance requirements per configuration. Table 7 reports the resulting power, the  $F_{max}$  achieved, and the minimum  $F_{max}$  (Target) required to meet the real-time requirements of each configuration. The achieved latency passes real-time constraints for  $CFG_{1\&2}$ , but fails for  $CFG_{3\&4}$ . Furthermore, since the dynamic power consumed is highly correlated with the size of a template,  $CFG_{2\&4}$  demonstrate drastic increases.

**Table 7: *Noema* implemented on a Stratix 10 FPGA.**

	$F_{max}$ (MHz)		Power (mW)		
	Achieved	Target	Static	Dynamic	Total
CFG1	467.51	30	5850.08	54.04	5904.12
CFG2	318.47	300	5860.47	1016.38	6876.85
CFG3	324.78	600	5851.42	495.03	6346.45
CFG4	258.53	900	5889.82	12014.81	17904.63

**Table 8: Pattern detection latency in ms on CPU & GPU. Real-time latency is 5ms. I/O time of transferring and binning the bitstreams is excluded. \* CFG did not fit on device.**

Device	CFG <sub>1</sub>	CFG <sub>2</sub>	CFG <sub>3</sub>	CFG <sub>4</sub>
<b>PCC Decomposition of Sections 3.1- 3.2</b>				
RPi3B	613	1455	12240	112952
i5 7000	63	257	1260	8605
GTX1080 - Manual	0.28	26.67	5.36	274.1
Jetson Nano - Manual	4.4	77.2	*	*
<b>Original PCC Formulation</b>				
GTX1080 - Thrust	1.20	4.27	3.96	20.6
Jetson Nano - Thrust	2.26	196	*	*
GTX1080 - Fast-GPU-PCC [22]	167.2	619.9	522.2	11395

### 5.4 Commodity Platforms: CPU and GPU

Software implementations of the PCC algorithm were implemented on a Raspberry Pi 3 Model B [8], an 8th generation Intel i5 laptop CPU [2] with 8 GB RAM, and NVIDIA’s Jetson Nano and GTX1080 GPUs [5, 7]. The CPU implementation uses a software pipeline to perform the binning and PCC calculations as per Subsection 3.1. Multiple configurations of data arrangements were tested with compiler flags set to infer SIMD operations where possible, and the best performing configuration was selected. Runtime and power usage are measured using an in-application timer and external power meter, respectively.

Multiple GPU implementations were evaluated on the Jetson Nano and GTX1080. The first was a hand-tuned implementation utilizing the same PCC decomposition and optimizations as in the CPU implementation. This performed the best for small configurations (e.g.,  $CFG_1$ ) reflective of current use cases. The second implementation follows the original formulation of PCC. It utilizes the Thrust (v1.8.3) library [12]. On the GTX1080, it outperforms the hand-tuned version in larger configurations ( $CFG_{2-4}$ ) but still fails to meet real-time expectations for  $CFG_4$ . However, given the GPU’s size and power consumption (10W/180W, respectively) [5, 6], an embedded solution would still be impractical. The last solution used the Fast-GPU-PCC algorithm [22] which converts PCC computation into a matrix multiplication problem. The parameters are emulated by substituting the number of voxels for neurons, and the length of time for the number of bins. The algorithm performs poorly even on the GTX1080, likely due to the differences in the problem setup. For all GPU solutions, we optimistically *exclude* the time needed to perform binning.

Table 8 summarizes the results. Both CPUs fail real-time latency needs for  $CFG_{1-4}$ , as does Fast-GPU-PCC. Raspberry Pi power was consistently measured at 2.4W, varying by <0.1 W. Achieving real-time latency of 5ms would require an improvement of 123 $\times$  for  $CFG_1$  and of 22,590 $\times$  for  $CFG_4$ . The laptop CPU performs significantly better, but still fails to meet latency requirements by a large margin. The desktop GPU can meet real-time requirements for  $CFG_{1-3}$ , but ultimately fails for  $CFG_4$  by 4 $\times$ . More recent GPUs would improve latency, however: a) energy would remain prohibitive, and b)  $PCC_{BASE}$  is a highly optimized GPU-like design which is more efficient for the particular application.

### ACKNOWLEDGMENTS

This work was supported by an NSERC Discovery Grant and the NSERC COHESA Strategic Research Network. The University of Toronto maintains all rights to the technologies described.

## REFERENCES

- [1] [n. d.]. Intan Technologies LLC, RHD2000 Series Digital Electrophysiology Interface Chips. [http://intantech.com/files/Intan\\_RHD2000\\_series\\_datasheet.pdf](http://intantech.com/files/Intan_RHD2000_series_datasheet.pdf). Accessed: 2020-11-17.
- [2] [n. d.]. Intel Intel®Core™i5-8265U Processor. <https://ark.intel.com/content/www/us/en/ark/products/149088/intel-core-i5-8265u-processor-6m-cache-up-to-3-90-ghz.html>. Accessed: 2020-6-18.
- [3] [n. d.]. Intel Quartus Prime Overview. <https://www.intel.ca/content/www/ca/en/software/programmable/quartus-prime/overview.html>. Accessed: 2020-4-17.
- [4] [n. d.]. Intel Stratix 10 Product Table. <https://www.intel.ca/content/dam/www/programmable/us/en/pdfs/literature/pt/stratix-10-product-table.pdf>. Accessed: 2020-4-17.
- [5] [n. d.]. NVIDIA GEFORCE GTX 1080. <https://www.nvidia.com/en-sg/geforce/products/10series/geforce-gtx-1080/>. Accessed: 2020-4-16.
- [6] [n. d.]. NVIDIA Jetson Linux Developer Guide (32.5 Release). [https://docs.nvidia.com/jetson/14t/index.html#page/Tegra%20Linux%20Driver%20Package%20Development%20Guide/power\\_management\\_nano.html#wpID0E0FLOHA](https://docs.nvidia.com/jetson/14t/index.html#page/Tegra%20Linux%20Driver%20Package%20Development%20Guide/power_management_nano.html#wpID0E0FLOHA). Accessed: 2021-6-20.
- [7] [n. d.]. NVIDIA Jetson Nano. <https://www.nvidia.com/en-us/autonomous-machines/embedded-systems/jetson-nano/education-projects/>. Accessed: 2021-6-20.
- [8] [n. d.]. RaspberryPi.org Raspberry Pi 3 Model B. <https://www.raspberrypi.org/products/raspberry-pi-3-model-b/>. Accessed: 2020-4-15.
- [9] Dayo O. Adewole, Laura A. Struzyna, Justin C. Burrell, James P. Harris, Ashley D. Nemes, Dmitriy Petrov, Reuben H. Kraft, H. Isaac Chen, Mijail D. Serruya, John A. Wolf, and D. Kacy Cullen. 2021. Development of optically controlled “living electrodes” with long-projecting axon tracts for a synaptic brain-machine interface. *Science Advances* 7, 4 (2021). <https://doi.org/10.1126/sciadv.aay5347> arXiv:<https://advances.sciencemag.org/content/7/4/eay5347.full.pdf>
- [10] Amos Arieli, Amiram Grinvald, and Hamutal Slovlin. 2002. Dural substitute for long-term imaging of cortical activity in behaving monkeys and its clinical implications. *Journal of Neuroscience Methods* 114, 2 (2002), 119–133. [https://doi.org/10.1016/S0165-0270\(01\)00507-6](https://doi.org/10.1016/S0165-0270(01)00507-6)
- [11] F. Arnaud, F. Boeuf, F. Salvetti, D. Lenoble, F. Wacquant, C. Regnier, P. Morin, N. Emonet, E. Denis, J. C. Oberlin, D. Ceccarelli, P. Vannier, G. Imbert, A. Sicard, C. Perrot, O. Belmont, I. Guilmeau, P. O. Sassoulas, S. Delmedico, R. Palla, F. Leverd, A. Beverina, V. DeJonghe, M. Broekaart, L. Pain, J. Todeschini, M. Charpin, Y. Laplanche, D. Neira, V. Vachellerie, B. Borot, T. Devoivre, N. Bicais, B. Hirschberger, R. Pantel, N. Revil, C. Parthasarathy, N. Planes, H. Brut, J. Farkas, J. Uginet, P. Stolk, and M. Woo. 2003. A functional 0.69  $\mu\text{m}^2/\text{sup} 2/$  embedded 6T-SRAM bit cell for 65 nm CMOS platform. In *2003 Symposium on VLSI Technology. Digest of Technical Papers (IEEE Cat. No.03CH37407)*. 65–66. <https://doi.org/10.1109/VLSIT.2003.1221088>
- [12] Nathan Bell and Jared Hoberock. 2012. *Thrust*. 359–371. <https://doi.org/10.1016/B978-0-12-385963-1.00026-5>
- [13] Edgar J. BermudezContreras, Andrea Gomez Palacio Schjetnan, Arif Muhammad, Peter Bartho, Bruce L. McNaughton, Bryan Kolb, Aaron J. Gruber, and Artur Luczak. 2013. Formation and reverberation of sequential neural activity patterns evoked by sensory stimulation are enhanced during cortical desynchronization. *Neuron* (2013). <https://doi.org/10.1016/j.neuron.2013.06.013>
- [14] Cadence. [n. d.]. Innovus Implementation System. [https://www.cadence.com/content/cadence-www/global/en\\_US/home/tools/digital-design-and-signoff/hierarchical-design-and-floorplanning/innovus-implementation-system.html](https://www.cadence.com/content/cadence-www/global/en_US/home/tools/digital-design-and-signoff/hierarchical-design-and-floorplanning/innovus-implementation-system.html)
- [15] John K. Chapin, Karen A. Moxon, Ronald S. Markowitz, and Miguel A.L. Nicolelis. 1999. Real-time control of a robot arm using simultaneously recorded neurons in the motor cortex. *Nature Neuroscience* (1999). <https://doi.org/10.1038/10223>
- [16] Sen Cheng and Loren M. Frank. 2008. New Experiences Enhance Coordinated Neural Activity in the Hippocampus. *Neuron* (2008). <https://doi.org/10.1016/j.neuron.2007.11.035>
- [17] Davide Ciliberti, Frédéric Michon, and Fabian Kloosterman. 2018. Real-time classification of experience-related ensemble spiking patterns for closed-loop applications. *eLife* (2018). <https://doi.org/10.7554/eLife.36275>
- [18] Davide Ciliberti, Frédéric Michon, and Fabian Kloosterman. 2018. Real-time classification of experience-related ensemble spiking patterns for closed-loop applications. *eLife* (Oct 2018). <https://doi.org/10.7554/eLife.36275>
- [19] Kelly Clancy, Aaron Koralek, Rui Costa, Daniel Feldman, and Jose Carmena. 2014. Volitional modulation of optically recorded calcium signals during neuroprosthetic learning. *Nature neuroscience* 17 (04 2014). <https://doi.org/10.1038/nn.3712>
- [20] Kamran Diba and György Buzsáki. 2007. Forward and reverse hippocampal place-cell sequences during ripples. *Nature Neuroscience* (2007). <https://doi.org/10.1038/nn1961>
- [21] Jean-Baptiste Eichenlaub, Beata Jarosiewicz, Jad Saab, Brian Franco, Jessica Kelemen, Eric Halgren, Leigh R. Hochberg, and Sydney S. Cash. 2020. Replay of Learned Neural Firing Sequences during Rest in Human Motor Cortex. *Cell Reports* 31, 5 (2020), 107581. <https://doi.org/10.1016/j.celrep.2020.107581>
- [22] Taban Eslami and Fahad Saeed. 2018. Fast-GPU-PCC: A GPU-Based Technique to Compute Pairwise Pearson’s Correlation Coefficients for Time Series Data – fMRI Study. *High-Throughput* 7, 2 (2018). <https://doi.org/10.3390/ht7020011>
- [23] David R. Euston, Masami Tatsuno, and Bruce L. McNaughton. 2007. Fast-forward playback of recent memory sequences in prefrontal cortex during sleep. *Science* (2007). <https://doi.org/10.1126/science.1148979>
- [24] David J. Foster and Matthew A. Wilson. 2006. Reverse replay of behavioural sequences in hippocampal place cells during the awake state. *Nature* (2006). <https://doi.org/10.1038/nature04587>
- [25] Luigi Galvani. 1791. *Aloysii Galvani De viribus electricitatis in motu musculari commentarius*. <https://doi.org/10.5479/sil.324681.39088000932442>
- [26] Yasser Ghanbari, Panos Papamichalis, and Larry Spence. 2009. Robustness of neural spike sorting to sampling rate and quantization bit depth. *2009 16th International Conference on Digital Signal Processing* (Jul 2009), 1–6. <https://doi.org/10.1109/ICDSP.2009.5201163>
- [27] R. Gnanasekaran. 1985. A Fast Serial-Parallel Binary Multiplier. *IEEE Trans. Comput.* 34, 08 (aug 1985), 741–744. <https://doi.org/10.1109/TC.1985.1676620>
- [28] S. Golomb. 1966. Run-length encodings (Corresp.). *IEEE Transactions on Information Theory* 12, 3 (1966), 399–401. <https://doi.org/10.1109/TIT.1966.1053907>
- [29] Igor Gridchyn, Philipp Schoenenberger, Joseph O’Neill, and Jozsef Csicsvari. 2020. Assembly-Specific Disruption of Hippocampal Replay Leads to Selective Memory Deficit. *Neuron* (2020). <https://doi.org/10.1016/j.neuron.2020.01.021>
- [30] Reid R Harrison. 2008. The design of integrated circuits to observe brain activity. *Proc. IEEE* 96, 7 (2008), 1203–1216.
- [31] HewlettPackard. [n. d.]. CACTI. <https://github.com/HewlettPackard/cacti>.
- [32] A. L. Hodgkin and A. F. Huxley. 1939. Action potentials recorded from inside a nerve fibre [8]. *Nature* (1939). <https://doi.org/10.1038/144710a0>
- [33] Sile Hu, Davide Ciliberti, Andres D. Grosmark, FrÅric Michon, Daoyuan Ji, Hector Penagos, GyÅrgy BuzsÅki, Matthew A. Wilson, Fabian Kloosterman, and Zhe Chen. 2018. Real-Time Readout of Large-Scale Unsorted Neural Ensemble Place Codes. *Cell Reports* 25, 10 (2018), 2635 – 2642.e5. <https://doi.org/10.1016/j.celrep.2018.11.033>
- [34] David H. Hubel. 1957. Tungsten microelectrode for recording from single units. *Science* (1957). <https://doi.org/10.1126/science.125.3247.549>
- [35] Daoyun Ji and Matthew A. Wilson. 2007. Coordinated memory replay in the visual cortex and hippocampus during sleep. *Nature Neuroscience* (2007). <https://doi.org/10.1038/nn1825>
- [36] James J. Jun, Nicholas A. Steinmetz, Joshua H. Siegle, Daniel J. Denman, Marius Bauza, Brian Barbarits, Albert K. Lee, Costas A. Anastassiou, Alexandru Andrei, Çağatay Aydın, Mladen Barbic, Timothy J. Blanche, Vincent Bonin, João C Couto, Barundeb Dutta, Sergey L. Gratiy, Diego A. Gutnisky, Michael HÅdusser, Bill Karsh, Peter Ledochowitsch, Carolina Mora Lopez, Catalin Mitelut, Silke Musa, Michael Okun, Marius Pachitariu, Jan Putzeys, P. Dylan Rich, Cyrille Rossant, Wei Lung Sun, Karel Svoboda, Matteo Carandini, Kenneth D. Harris, Christof Koch, John O’Keefe, and Timothy D. Harris. 2017. Fully integrated silicon probes for high-density recording of neural activity. *Nature* 551, 7679 (2017), 232–236. <https://doi.org/10.1038/nature24636>
- [37] Mattias P. Karlsson and Loren M. Frank. 2009. Awake replay of remote experiences in the hippocampus. *Nature Neuroscience* (2009). <https://doi.org/10.1038/nn.2344>
- [38] E. Kijispongse, S. U-ruekolan, C. Ngamphiw, and S. Tongsimma. 2011. Efficient large Pearson correlation matrix computing using hybrid MPI/CUDA. In *2011 Eighth International Joint Conference on Computer Science and Software Engineering (JCSSE)*. 237–241.
- [39] Tony Hyun Kim, Yanping Zhang, JÅrÅme Lecoq, Juergen C. Jung, Jane Li, Hongkui Zeng, Christopher M. Niell, and Mark J. Schnitzer. 2016. Long-Term Optical Access to an Estimated One Million Neurons in the Live Mouse Cortex. *Cell Reports* (2016). <https://doi.org/10.1016/j.celrep.2016.12.004>
- [40] Tony Hyun Kim, Yanping Zhang, Jérôme Lecoq, Juergen C. Jung, Jane Li, Hongkui Zeng, Christopher M. Niell, and Mark J. Schnitzer. 2016. Long-Term Optical Access to an Estimated One Million Neurons in the Live Mouse Cortex. *Cell Rep.* 17, 12 (Dec 2016), 3385–3394. <https://doi.org/10.1016/j.celrep.2016.12.004>
- [41] Hemant S. Kudrimoti, Carol A. Barnes, and Bruce L. McNaughton. 1999. Reactivation of hippocampal cell assemblies: Effects of behavioral state, experience, and EEG dynamics. *Journal of Neuroscience* (1999). <https://doi.org/10.1523/jneurosci.19-10-04090.1999>
- [42] M A Lebedev, J M Carmena, and M A Nicolelis. 2003. Directional tuning of frontal and parietal neurons during operation of brain - machine interface. *Society for Neuroscience Abstract Viewer and Itinerary Planner* (2003).
- [43] Albert K. Lee and Matthew A. Wilson. 2002. Memory of sequential experience in the hippocampus during slow wave sleep. *Neuron* (2002). [https://doi.org/10.1016/S0896-6273\(02\)01096-6](https://doi.org/10.1016/S0896-6273(02)01096-6)
- [44] Meimei Liang, Futao Zhang, Gulei Jin, and Jun Zhu. 2015. FastGCN: A GPU Accelerated Tool for Fast Gene Co-Expression Networks. *PLOS ONE* 10, 1 (01 2015), 1–11.
- [45] Bengt Ljungquist, Per Petersson, Anders J. Johansson, Jens Schouenborg, and Martin Garwicz. 2018. A Bit-Encoding Based New Data Structure for Time and Memory Efficient Handling of Spike Times in an Electrophysiological Setup. *Neuroinformatics* 16, 2 (Apr 2018), 217–229. <https://doi.org/10.1007/s12021-018-9367-z> arXiv:29508123

- [46] Kenway Louie and Matthew A. Wilson. 2001. Temporally structured replay of awake hippocampal ensemble activity during rapid eye movement sleep. *Neuron* (2001). [https://doi.org/10.1016/S0896-6273\(01\)00186-6](https://doi.org/10.1016/S0896-6273(01)00186-6)
- [47] Song Luan, Ian Williams, Michal Maslik, Yan Liu, Felipe de Carvalho, Andrew Jackson, Rodrigo Quiñan Quiroga, and Timothy G. Constantinou. 2017. Compact Standalone Platform for Neural Recording with Real-Time Spike Sorting and Data Logging. *bioRxiv* (2017). <https://doi.org/10.1101/186627> arXiv:<https://www.biorxiv.org/content/early/2017/09/22/186627.1.full.pdf>
- [48] Artur Luczak, Peter Barthó, and Kenneth D. Harris. 2009. Spontaneous Events Outline the Realm of Possible Sensory Responses in Neocortical Populations. *Neuron* (2009). <https://doi.org/10.1016/j.neuron.2009.03.014>
- [49] Jason N. MacLean, Brendon O. Watson, Gloster B. Aaron, and Rafael Yuste. 2005. Internal dynamics determine the cortical response to thalamic stimulation. *Neuron* (2005). <https://doi.org/10.1016/j.neuron.2005.09.035>
- [50] E. M. Maynard, N. G. Hatsopoulos, C. L. Ojakangas, B. D. Acuna, J. N. Sanes, R. A. Normann, and J. P. Donoghue. 1999. Neuronal interactions improve cortical population coding of movement direction. *Journal of Neuroscience* (1999). <https://doi.org/10.1523/jneurosci.19-18-08083.1999>
- [51] Ethan M Meyers, Mia Borzello, Winrich A Freiwald, and Doris Tsao. 2015. Intelligent information loss: the coding of facial identity, head pose, and non-face information in the macaque face patch system. *Journal of Neuroscience* 35, 18 (2015), 7069–7081.
- [52] Robbin A. Miranda, William D. Casebeer, Amy M. Hein, Jack W. Judy, Eric P. Krotkov, Tracy L. Laabs, Justin E. Manzo, Kent G. Pankratz, Gill A. Pratt, Justin C. Sanchez, Douglas J. Weber, Tracy L. Wheeler, and Geoffrey S.F. Ling. 2015. DARPA-funded efforts in the development of novel brain-computer interface technologies. *Journal of Neuroscience Methods* 244 (2015), 52–67. <https://doi.org/10.1016/j.jneumeth.2014.07.019> Brain Computer Interfaces; Tribute to Greg A. Gerhardt.
- [53] Elon Musk and Neuralink. 2019. An integrated brain-machine interface platform with thousands of channels. *bioRxiv* (2019). <https://doi.org/10.1101/703801> arXiv:<https://www.biorxiv.org/content/early/2019/08/02/703801.full.pdf>
- [54] Z. Nadasdy, H. Hirase, A. Czurko, J. Csicsvari, and G. Buzsáki. 1999. Replay and time compression of recurring spike sequences in the hippocampus [In Process Citation]. *J Neurosci* (1999).
- [55] S. Natarajan, M. Agostinelli, S. Akbar, M. Bost, A. Bowonder, V. Chikarmane, S. Chouksey, A. Dasgupta, K. Fischer, Q. Fu, T. Ghani, M. Giles, S. Govindaraju, R. Grover, W. Han, D. Hanken, E. Haralson, M. Haran, M. Heckscher, R. Heussner, P. Jain, R. James, R. Jhaveri, I. Jin, H. Kam, E. Karl, C. Kenyon, M. Liu, Y. Luo, R. Mehandru, S. Morarka, L. Neiberg, P. Packan, A. Paliwal, C. Parker, P. Patel, R. Patel, C. Pelto, L. Pipes, P. Plekhanov, M. Prince, S. Rajamani, J. Sandford, B. Sell, S. Sivakumar, P. Smith, B. Song, K. Tone, T. Troeger, J. Wiedemer, M. Yang, and K. Zhang. 2014. A 14nm logic technology featuring 2nd-generation FinFET, air-gapped interconnects, self-aligned double patterning and a 0.0588 Åtm2 SRAM cell size. In *2014 IEEE International Electron Devices Meeting*. 3.7.1–3.7.3. <https://doi.org/10.1109/IEDM.2014.7046976>
- [56] Joaquin Navajas, Deren Y Barsakcioglu, Amir Eftekhari, Andrew Jackson, Timothy G Constantinou, and Rodrigo Quiñan Quiroga. 2014. Minimum requirements for accurate and efficient real-time on-chip spike sorting. *Journal of neuroscience methods* 230 (2014), 51–64.
- [57] Arto Nurmi, David Borton, and Ming Yin. 2016. *Wireless Neurotechnology for Neural Prostheses*. John Wiley & Sons, Ltd, Chapter 5, 123–161. <https://doi.org/10.1002/9781118816028.ch5> arXiv:<https://onlinelibrary.wiley.com/doi/pdf/10.1002/9781118816028.ch5>
- [58] H. Freyja Ólafsdóttir, Francis Carpenter, and Caswell Barry. 2016. Coordinated grid and place cell replay during rest. *Nature Neuroscience* (2016). <https://doi.org/10.1038/nn.4291>
- [59] Stefano Panzeri, Jakob H. Macke, Joachim Gross, and Christoph Kayser. 2015. Neural population coding: Combining insights from microscopic and mass signals. *Trends in Cognitive Sciences* (2015). <https://doi.org/10.1016/j.tics.2015.01.002>
- [60] Alexandre Pouget, Peter Dayan, and Richard Zemel. 2000. Information processing with population codes. *Nature Reviews Neuroscience* (2000). <https://doi.org/10.1038/35039062>
- [61] E. Reggiani, E. D’Arnese, A. Purgato, and M. D. Santambrogio. 2017. Pearson Correlation Coefficient Acceleration for Modeling and Mapping of Neural Interconnections. In *2017 IEEE International Parallel and Distributed Processing Symposium Workshops (IPDPSW)*. 223–228.
- [62] Sidarta Ribeiro, Damien Gervasoni, Ernesto S. Soares, Yi Zhou, Shih Chieh Lin, Janaina Pantoja, Michael Lavine, and Miguel A.L. Nicolelis. 2004. Long-lasting novelty-induced neuronal reverberation during slow-wave sleep in multiple forebrain areas. *PLoS Biology* (2004). <https://doi.org/10.1371/journal.pbio.0020024>
- [63] R. Rice and J. Plaunt. 1971. Adaptive Variable-Length Coding for Efficient Compression of Spacecraft Television Data. *IEEE Transactions on Communication Technology* 19, 6 (1971), 889–897. <https://doi.org/10.1109/TCOM.1971.1090789>
- [64] B. Rooseleer, S. Cosemans, and W. Dehaene. 2011. A 65 nm, 850 MHz, 256 kbit, 4.3 pJ/access, ultra low leakage power memory using dynamic cell stability and a dual swing data link. In *2011 Proceedings of the ESSCIRC (ESSCIRC)*. 519–522. <https://doi.org/10.1109/ESSCIRC.2011.6044936>
- [65] Mijail D. Serruya, Nicholas G. Hatsopoulos, Liam Paninski, Matthew R. Fellous, and John P. Donoghue. 2002. Instant neural control of a movement signal. *Nature* 416, 6877 (2002), 1414–1418. <https://doi.org/10.1038/416141a>
- [66] Robert K Shepherd. 2016. *Neurobionics: The biomedical engineering of neural prostheses*. John Wiley & Sons.
- [67] P. Socha, V. Miškovský, H. Kubátová, and M. Novotný. 2017. Optimization of Pearson correlation coefficient calculation for DPA and comparison of different approaches. In *2017 IEEE 20th International Symposium on Design and Diagnostics of Electronic Circuits Systems (DDECS)*. 184–189.
- [68] T. Song, W. Rim, J. Jung, G. Yang, J. Park, S. Park, K. Baek, S. Baek, S. Oh, J. Jung, S. Kim, G. Kim, J. Kim, Y. Lee, K. S. Kim, S. Sim, J. S. Yoon, and K. Choi. 2014. 13.2 A 14nm FinFET 128Mb 6T SRAM with VMIN-enhancement techniques for low-power applications. In *2014 IEEE International Solid-State Circuits Conference Digest of Technical Papers (ISSCC)*. 232–233. <https://doi.org/10.1109/ISSCC.2014.6757413>
- [69] Ethan Sorrell, Michael E. Rule, and Timothy O’Leary. 2021. Brain-Machine Interfaces: Closed-Loop Control in an Adaptive System. *Annual Review of Control, Robotics, and Autonomous Systems* 4, 1 (2021), null. <https://doi.org/10.1146/annurev-control-061720-012348>
- [70] Hendrik Steenland and Bruce L. McNaughton. 2015. Techniques for Large-Scale Multiunit Recording. In *Analysis and Modeling of Coordinated Multi-neuronal Activity*. Springer. <https://doi.org/10.1007/978-1-4939-1969-7>
- [71] Nick Steinmetz, Marius Pachitariu, Carsen Stringer, Matteo Carandini, and Kenneth Harris. 2019. Eight-probe Neuropixels recordings during spontaneous behaviors. <https://doi.org/10.25378/janelia.7739750.v4>
- [72] Carsen Stringer, Marius Pachitariu, Nicholas Steinmetz, Charu Bai Reddy, Matteo Carandini, and Kenneth D. Harris. 2019. Spontaneous behaviors drive multidimensional, brainwide activity. *Science* (2019). <https://doi.org/10.1126/science.aav7893>
- [73] Synopsys. [n. d.]. Design Compiler Graphical. <https://www.synopsys.com/implementation-and-signoff/rtl-synthesis-test/design-compiler-graphical.html>
- [74] M. Tatsuno, P. Lipa, and B. L. McNaughton. 2006. Methodological Considerations on the Use of Template Matching to Study Long-Lasting Memory Trace Replay. *Journal of Neuroscience* (2006). <https://doi.org/10.1523/JNEUROSCI.3317-06.2006>
- [75] Masami Tatsuno, Soroush Malek, LeAnna Kalvi, Adrian Ponce-Alvarez, Karim Ali, David R. Euston, Sonja Grün, and Bruce L. McNaughton. 2020. Memory reactivation in rat medial prefrontal cortex occurs in a subtype of cortical UP state during slow-wave sleep. *Phil. Trans. R. Soc. B* 375, 1799 (May 2020). <https://doi.org/10.1098/rstb.2019.0227>
- [76] Patrick Tresco and Brent Winslow. 2011. The Challenge of Integrating Devices into the Central Nervous System. *Critical reviews in biomedical engineering* 39 (01 2011), 29–44. <https://doi.org/10.1615/CritRevBiomedEng.v39.i1.30>
- [77] Bing Wang, Pengbo Yang, Yaxue Ding, Honglan Qi, Qiang Gao, and Chengxiao Zhang. 2019. Improvement of the Biocompatibility and Potential Stability of Chronically Implanted Electrodes Incorporating Coating Cell Membranes. *ACS Applied Materials & Interfaces* 11, 9 (2019), 8807–8817. <https://doi.org/10.1021/acsami.8b20542> PMID: 30741520.
- [78] Pan Ke Wang, Sio Hang Pun, Chang Hao Chen, Elizabeth A. McCullagh, Achim Klug, Anan Li, Mang I. Vai, Peng Un Mak, and Tim C. Lei. 2019. Low-latency single channel real-time neural spike sorting system based on template matching. *PLOS ONE* 14, 11 (11 2019), 1–30. <https://doi.org/10.1371/journal.pone.0225138>
- [79] Keita Watanabe, Tatsuya Haga, Masami Tatsuno, David R. Euston, and Tomoki Fukai. 2019. Unsupervised Detection of Cell-Assembly Sequences by Similarity-Based Clustering. *Frontiers in Neuroinformatics* 13 (2019), 39. <https://doi.org/10.3389/fninf.2019.00039>
- [80] Siegfried Weisenburger and Alipasha Vaziri. 2018. A Guide to Emerging Technologies for Large-Scale and Whole-Brain Optical Imaging of Neuronal Activity. *Annual Review of Neuroscience* (2018). <https://doi.org/10.1146/annurev-neuro-072116-031458>
- [81] Aaron A. Wilber, Ivan Skelin, Wei Wu, and Bruce L. McNaughton. 2017. Laminar Organization of Encoding and Memory Reactivation in the Parietal Cortex. *Neuron* 95, 6 (13 Sep 2017), 1406–1419.e5. <https://doi.org/10.1016/j.neuron.2017.08.033> 28910623[pmid].
- [82] I. Williams, S. Luan, A. Jackson, and T. G. Constantinou. 2015. Live demonstration: A scalable 32-channel neural recording and real-time FPGA based spike sorting system. In *2015 IEEE Biomedical Circuits and Systems Conference (BioCAS)*. 1–5. <https://doi.org/10.1109/BioCAS.2015.7348330>
- [83] Yaniv Ziv, Laurie D. Burns, Eric D. Cocker, Elizabeth O. Hamel, Kunal K. Ghosh, Lacey J. Kitch, Abbas El Gamal, and Mark J. Schnitzer. 2013. Long-term dynamics of CA1 hippocampal place codes. *Nature Neuroscience* 16, 3 (Mar 2013), 264–266. <https://doi.org/10.1038/nn.3329>